Laser and Particle Beams

cambridge.org/lpb

Contaminant-free alpha particles signature from laser-driven proton-boron fusion plasma using Thomson parabola spectrometer

Aaron McNamee[1], Vasiliki Kantarelou[2], Gagik Nersisyan[1], Alessandro Milani[3], Alessandro Maffini[3], Davide Orecchia[3], Philip Martin[1], Massimiliano Scisciò[4], Lorenzo Giuffrida[2], Fabrizio Consoli[4], Satyabrata Kar[1], Daniele Margarone[1,2]

[1]Centre For Light-Matter Interactions, Queen's University Belfast, Belfast, UK; [2]ELI Beamlines Facility, The Extreme Light Infrastructure ERIC, Dolni Brezany, Czech Republic; [3]Politecnico di Milano, Milan, Italy and [4]ENEA Nuclear Department – C. R. Frascati, Via Enrico Fermi 45, Frascati, Italy

Research Article

Cite this article: McNamee A *et al*. (2025) Contaminant-free alpha particles signature from laser-driven proton-boron fusion plasma using Thomson parabola spectrometer. *Laser and Particle Beams* **43**, e8, 1–12. https://doi.org/10.1017/lpb.2025.10005

Received: 11 May 2025
Revised: 20 August 2025
Accepted: 16 September 2025

Keywords:
alpha; diagnostic; fusion; proton-boron

Corresponding author: Aaron McNamee;
Email: amcnamee08@qub.ac.uk

Abstract

Accurate discrimination and energy measurement of alpha particles remain a key challenge in proton boron fusion driven by high-intensity laser-plasma interaction due to the complex mix of ions generated in these extreme conditions. We present a novel implementation of a high-accuracy, low-background technique involving a CR-39 enhanced image plate that was used with a Thomson parabola spectrometer (TPS) and differential filtering. This technique demonstrated a strong reduction in background contamination arising from plasma ions compared to standard CR-39 and allowed for the generation of a contaminant-free alpha particle energy spectrum from a boron foam target irradiated by a 10 J, 800 fs laser pulse with an intensity of $\sim 2 \times 10^{19}\ Wcm^{-2}$. The laser pulse was from a hybrid Ti:Sapphire-Nd:glass system generated from the Chirped Pulse Amplification (CPA) mode. The spectrum covered an energy range of 3–8 MeV with a corresponding energy resolution of 0.1–0.5 MeV. The developed filtering technique has the potential to measure even lower energy ranges, further extending its applicability compared with existing methods. The differential filtering solution strongly reduces the signal from carbon ions that would otherwise overlap the alpha particle trace on the TPS, providing a quasi-contaminant-free signal, while the CR-39 enhanced the detection sensitivity compared to other detectors.

Introduction

The field of nuclear fusion is experiencing significant momentum, bolstered by billions in private sector funding (Refs 34, 48) and continued advances in the field, such as breaking previous records (Ref 55). The potential of machine learning to further accelerate progress, for instance by improving plasma containment (Ref 50) or optimising laser pulse temporal profiles (Ref 52), adds to this outlook. As a result, fusion technology appears poised to hit an inflexion point and contribute to addressing the climate crisis. With the renewed interest, novel approaches to the concept are also receiving increased attention beyond the traditional approach of a magnetic confinement tokamak reactor using a deuterium and tritium fuel (Refs 6, 23, 31). One such approach is inertial confinement fusion using proton-boron fuel (Ref 30).

While commercialisation of fusion power has not yet been achieved, several challenges associated with traditional D-T fusion have already been identified as barriers to deployment. One major concern is the high neutron production in D-T plasma, where the primary reaction yields a significant number of neutrons. These neutrons can degrade reactor containment vessel walls (Ref 38), create radioactive waste, and result in substantial energy loss, as their energy is difficult to extract for electricity generation (Ref 51). In contrast, aneutronic fuels like proton-boron (p-11B) offer advantages by producing only a minimal amount of neutrons, around 0.1%(Ref 32) of the total reactions in the plasma. The p-11B reaction predominantly generates alpha particles, which are easier to utilise for energy extraction.

Deuterium, as a fuel, is relatively abundant in seawater (Ref 16), making extraction feasible. However, tritium is more difficult to deal with due to its radioactive nature with a half-life of 12.3 years (Ref 24) and poses the additional challenge of the majority of global production relying on nuclear reactor moderator pools (Refs 35, 40). Current global tritium production is estimated at only 20 kg per year (Ref 39). However, a reactor like DEMO would require 300 grams daily, highlighting the need for alternative solutions (Ref 18). One proposed solution, the use of a lithium blanket for in-situ tritium production, remains unproven (Ref 43). On the other hand, boron, required for proton-boron fusion, has a yearly production estimate of

830,000 tons (Ref 37), making it readily available. Beyond power generation, proton-boron fusion also holds potential in radioisotope production (Refs 22, 41, 42) and as a medical treatment for cancer (Ref 8). One example is Proton Boron Capture Therapy (PBCT), where a targeted proton beam induces localised boron reactions, releasing high-Let alpha particles for precise tumour cell destruction (Ref 54). However, a key challenge in laser-driven p-11B research lies in the accurate discrimination and measurement of alpha particles in an intense and multi-particle species plasma radiation environment (Ref 10).

Accurate discrimination and measurement of alpha particles in laser-driven p-11B experiments is crucial for understanding the reaction dynamics and optimising the fusion process. However, the complex mix of ions generated in these extreme conditions poses a significant challenge for traditional diagnostic techniques. Solid-state nuclear track detectors, such as CR-39, have been widely used in laser-driven fusion experiments due to their high sensitivity to individual particles and insensitivity to electromagnetic radiation (Refs 7, 10, 57). CR-39 detectors can provide valuable information on the spatial distribution and flux of alpha particles, but they have limitations in terms of energy resolution and particle discrimination (Ref 10).

To overcome these issues, this paper will focus on a novel approach of combining CR-39 detectors, a Thomson parabola spectrometer (TPS) (Ref 53) and foil filters. TPS is a powerful diagnostic tool that uses parallel electric and magnetic fields to disperse a beam of collimated charged particles based on their energy and charge-to-mass ratio, producing distinct parabolic traces on a detector plane (Ref 2). By coupling CR-39 detectors with a TPS and employing differential filtering techniques with foil filters, we aim to achieve high-resolution, contaminant-free alpha particle measurements in laser-driven p-11B experiments.

Differential filters (Ref 45) is a technique that takes advantage of the stopping power of different particles by layering filters of different thicknesses on top of each other in such a way as to maintain an effective thickness along the entire trace produced on the TPS that blocks heavy ions that are predicted to hit a given spot while remaining thin enough to allow alpha particles to penetrate through. This is crucial due to fully ionised carbon-12, a common product in laser-plasma experiments, due to hydrocarbon contaminants on the target surface, having the same charge-to-mass ratio as alpha particles and thus overlapping the alpha particles' trace, making it difficult to discern the respective contributions to the signal.

There has been discussion in the past of the different diagnostics techniques for alpha particle detection for p-11B fusion, such as Consoli et al (Ref 10). These explored all the components of the technique that is the focus of the paper like TPS, CR-39 and filters, however, the advantage of them in concert was not discussed. Instead, the majority of experiments used CR-39 (Refs 5, 13, 15, 47) to detect alpha due to its reliability in harsh laser-plasma conditions, then supplementing these results with data from Time of Flight detectors. The first mention of a technique similar to the one employed in this paper was in 2014 by Alejo et al (Ref 1), which demonstrated this approach to discriminate laser-accelerated deuterium ions from overlapping heavier species of ions by using filters of varying thickness along the energy dispersion axis of the TPS. Papers that used a similar method were by Kantarelou et al (Ref 21) and Baccou et al (Ref 3), who used a CR-39 coupled with a TPS to calibrate CR-39 detectors for low-energy plasma ions in proton-boron fusion experiments. Finally, recently, Salvadori et al (Ref 45) proposed a concept similar in principle to using differential filters with TPS; however, no experimental data were presented, and the concept would not have acquired some of the information from the alpha particles due to the filter frame blocking some energies. In this paper, we present for the first time an experiment that combines these techniques to obtain a high-resolution, contaminant-free alpha particle signature from a laser-driven p-11B fusion reaction.

Methods

The experiment used the TARANIS laser at Queen's University Belfast. This is a hybrid Ti:Sapphire-Nd:glass system operating in the Chirped Pulse Amplification (CPA) mode, working at a wavelength of 1053 nm and a nominal energy of 10 J with an average pulse length of 800 fs, producing a linearly polarised laser. The laser had a recorded average energy of 9.3 ± 1.6 J during the experiment. The laser also irradiated targets at an angle of 20°, generating a stream of multi-species ions of a broad energy spectrum. The laser was focused onto a focal spot with a full width at half maximum (FWHM) of 5.1 μm with an average intensity of 2×10^{19} Wcm^{-2} across the FWHM.

The targets used were a boron nitride target (BN), a boron high-density polyethylene (HDPE) foam target (B+CH) and a double-layer aluminium polyethylene target (Al+CH) that were all set up for the single target configuration, wherein the target is composed of a single component (Ref 29). These targets were designed with an in-target geometry (Ref 26), where the laser irradiation and the fusion process occur within the same target structure. The BN target had a thickness of 1.5 mm. The B+CH target was made up of a 1 mm thick layer of polypropylene to act as a substrate, then a boron foam layer made up of boron, polyethylene and hydrogen. This boron foam layer had a thickness of 60 μm, a density of 80 mg/cm^3 and a hydrogen content of 2.8×10^{21} cm^{-3} or a ratio of H/B∼1.4(Ref 36). Lastly, the Al+CH was a 10 μm thick layer of polypropylene, then an 11 μm thick layer of aluminium. Both the BN and B+CH targets were used to produce alpha particles. Alternatively, the purpose of the Al+CH target would be to produce no alpha particles and could be used to produce a reference (background) result for the B+CH target.

To validate alpha particle detection on the novel diagnostic, three CR-39 detectors were positioned around the target at angles of 80°, 45° and −44° relative to the target surface normal. The distances between the CR-39 detectors and the target varied depending on the interaction chamber operating mode to ensure that overlapping of pits did not occur, i.e. saturation of the detector did not occur. For single-shot operation, the detectors were placed at distances of 450, 500 and 490 mm, respectively. In accumulating-shot mode, these distances were increased to 640, 700 and 670 mm, respectively.

The Thomson Parabola Spectrometer (TPS) component of the novel diagnostic was employed to analyse the ions emitted. The TPS was placed facing the front exposed surface of the target at an angle of 60°. with respect to the target normal at a distance of 155 mm. This angle was selected to accommodate the interaction chamber constraints and optimise ion detection based on prior observations of high alpha particles but low plasma ions emission patterns (Refs 13, 27).

The overall experimental configuration, including the target chamber, diagnostic placements, and key spectrometer dimensions, is illustrated in Figure 1. Specifically, Figure 1(a) provides a schematic overview of the experimental setup in the interaction

https://doi.org/10.1017/lpb.2025.10005 Published online by Cambridge University Press

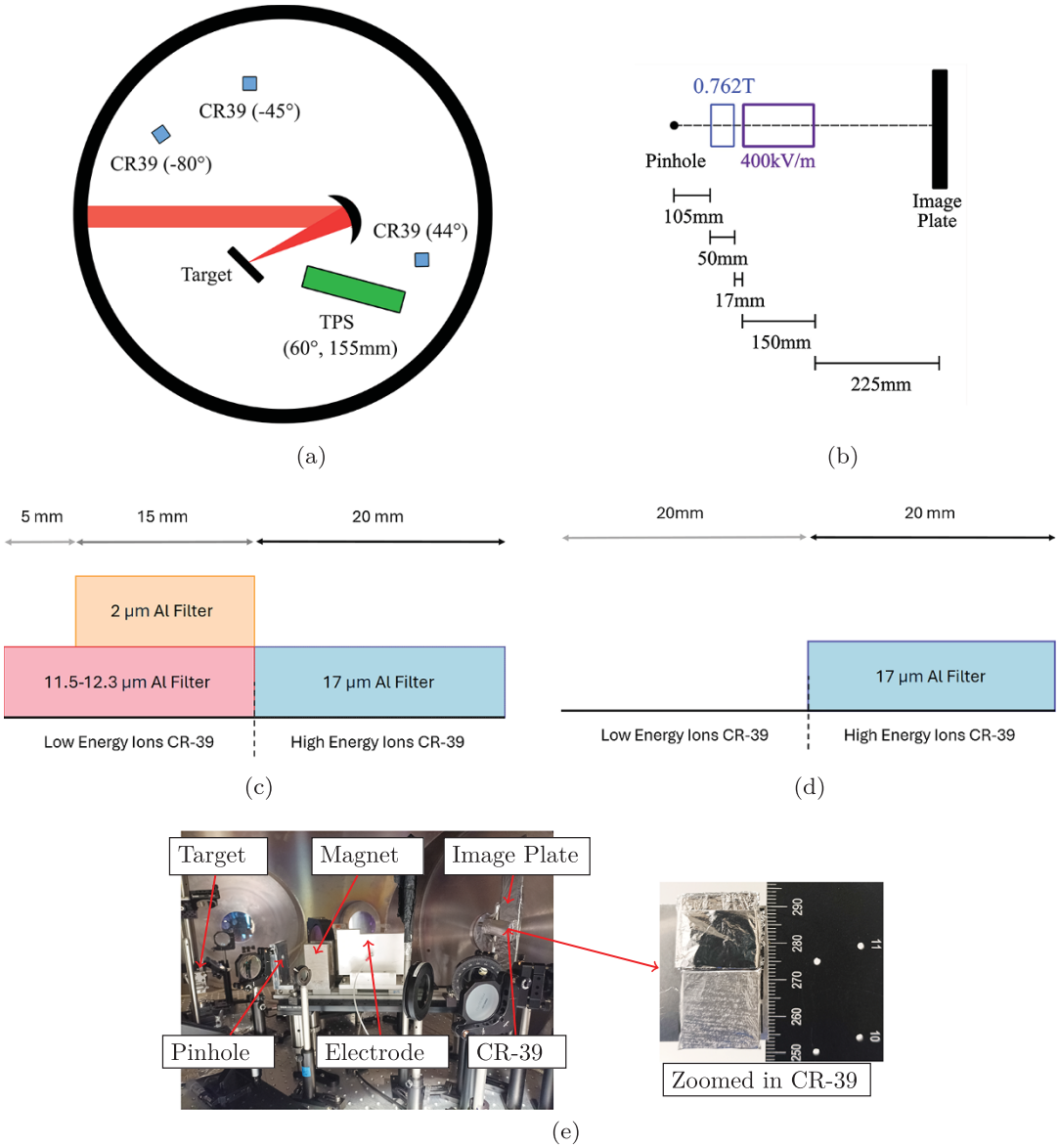

Figure 1. Diagrams and pictures showing the setup of the experiment with (a) a representative diagram of the TARANIS experimental setup, (b) a diagram of the dimensions of the Thomson Parabola Spectrometer with the magnetic field outlined in blue and the electric field outlined in purple, (c) a diagram of the filter setup for the CR-39s used for the Boron HDPE Foam target (d) a diagram of the filter setup for the CR-39s used for the Boron Nitride target and (e) a labelled picture of interaction chamber with the Thomson Parabola installed along with the image plate and CR-39 in front of that along with a zoomed-in picture showing the CR-39s with the filters used for the Boron HDPE Foam target (a) Labelled diagram of experimental setup, (b) Thomson parabola diagram, (c) Boron HDPE foam target filter setup, (d) Boron Nitride Target Filter Setup, (e) Labelled Photo of Experimental Setup.

chamber, while Figure 1(b) details the geometry of the TPS itself. Laser-driven ions from the target were collimated by a large 600 μm diameter pinhole. This approach was chosen to increase the number of alpha particles entering the TPS. However, the trade-off was a reduced energy resolution of the detector. This reduction was due to the magnification inherent in the pinhole projection, which resulted in the ions forming a visually observed 1.36 mm wide trace on the image plate (Ref 53), broadening the detected energy features. The ions were deflected along the y-axis (corresponding to the vertical axis of the interaction chamber) by the magnetic field of the TPS according to their energy, following the equation (1) shown below (Ref 2). The strength of the magnetic field was initially intended to be calibrated using a Fujifilm image plate detector to measure the proton trace, which allowed for a measurement of the magnetic field using the location of the cut-off point of protons on the 6.5 μm aluminium filter covering the entire image plate with a predicted energy of 0.57 MeV according to SRIM simulation (Ref 19). Simultaneously, the electric field of the TPS, on the other hand, deflected the particles in a perpendicular direction along the x-axis according to their charge-to-mass ratio with a field strength of 400 kV/m according to the equation (2) shown below (Ref 2).

$$y = \frac{qB_0L_B}{m_0v}(L_B/2 + D_B), \tag{1}$$

$$x = \frac{qE_0L_E}{m_0v^2}(T_E - L_E/2). \tag{2}$$

https://doi.org/10.1017/lpb.2025.10005 Published online by Cambridge University Press

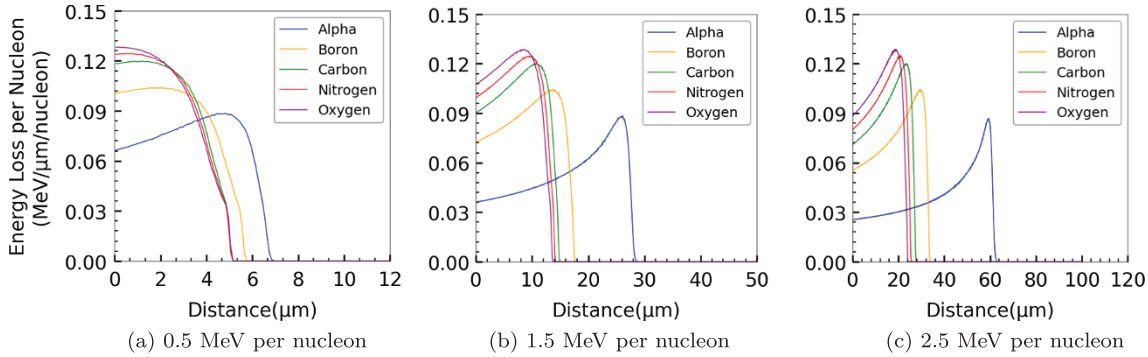

Figure 2. Graphs showing the energy deposition and penetration depth of particles likely to be produced in a laser-plasma experiment. The target material is aluminium. Each graph represents a different energy per nucleon, calculated using SRIM. (a) 0.5 MeV per nucleon, (b) 1.5 MeV per nucleon, (c) 2.5 MeV per nucleon.

The meaning of the terms in the equation are as follows, q and m_0 are the charge and rest mass of the species of ion; v is the particle's velocity; L_B and D_B denote the magnetic field length and drift distance to the detector from the end of the field; L_E and T_E are the electric field length and drift distance; B_0 and E_0 are the magnetic and electric field strengths; and c is the speed of light.

Although the electric field strength was set to 400 kV/m the actually measured value was closer to 340 kV/m. This has been observed in previous experiments (Ref 9) and may be due to field fringing effects or the electron currents, which arrive before the positive ions, cancelling out the positive electrode. The TPS is set up in the interaction chamber and shown photographically in Figure 1(e) along with the CR-39 with filters on it.

The image plate was enhanced by the addition of the CR-39 component of the novel technique, covering part of the parabola trace produced, particularly in the region expected to detect the highest alpha flux. This was based on previous literature (Refs 13, 17, 47) showing a peak alpha particle flux in the 2–7 MeV range for p-11B fusion. The CR-39 detector was then positioned using the Thomson parabola equations to specifically intercept this energy range. The CR-39 used for the TPS was fixed to a separate holder and then placed flush against the image plate. The image plate was intended to be covered in a 6.5 μm thick Al foil to limit exposure to ambient light after irradiation. The image plate serves two important purposes. First, it confirms that a successful shot was made on the target, indicating that a signal is likely to be detected on the CR-39. Second, it helps provide a more accurate positioning of the CR-39 in relation to the zero point (i.e., undeflected X-rays generated in the laser-plasma interaction). The shadow produced by the CR-39 on the image plate can then act as a calibration, helping determine the energy levels of the pits seen after etching.

Aluminium was selected as the optimal material for differential foil filters based on three key criteria. First, it effectively discriminates between alpha particles and carbon ions via differing penetration depths at relevant energies, supported by SRIM energy deposition simulation data in Figure 2. Second, the reliability of SRIM predictions for aluminium is validated by excellent agreement with experimental data (Ref 19). Third, suitable aluminium foils are commercially available and cost-effective.

The differential filters used on the CR-39 for the experiment had nominal values of two thicknesses, 2 μm and 6.5 μm, provided by the manufacturer. The manufacturer gave a 30% uncertainty for the actual thickness of the foils. The foils also, due to how thin foils are manufactured, can have a condition called not light tight. This means that pinholes may be present across the surface of the material, which could be detrimental to the success of the technique. This was not an issue for this experiment due to the alpha particle trace (cm) being much wider than the pinholes (μm), meaning any pinholes present in the path of the trace would constitute only a small proportion of the area covered, allowing only a negligible amount of carbon ions through. The full filter setup, as seen in Figure 1(c), consisted of two CR-39 detectors.

The bottom CR-39 was covered in two nominal 6.5 μm foils totalling an intended 13 μm for the higher energy particles and the CR-39 placed above it was to be wrapped in a 6.5 μm foil with a 2 μm foil covering the bottom 15 mm for an effective thickness of 8.5 μm. This was designed to nearly fully eliminate any carbon signal across the entire energy spectrum and was used for the B+CH target.

This meant that the accuracy of the energy spectrum generated was largely limited by the accuracy of the TPS setup used and not the number of filters used, as in traditional CR-39 setups. According to the TP equation (1) and the assumed strength of the magnetic field, these energies translated to locations were 6.5 μm for 5 mm, then 8.5 μm for 15 mm and finally 13 μm for the remaining available area with the top of the CR-39 intended to be positioned 71 mm away from the zero point. The position of the filters, both concerning the CR-39 and the alpha particle trace produced by the TPS, is important to achieve the desired result and needs to be tailored for the parameters of the TPS used. The multilayer filter configuration, shown in Figure 1(c), was designed for specific energy ranges.

However, initial analysis of the image plate revealed a significant positioning error of the CR-39 detector, which was located 8 mm closer to the zero point than intended (63 mm actual vs 71 mm planned). The 8 mm positioning error was caused by the mechanical instability of the ad-hoc holder for the CR-39 detector. The setup, which involved attaching the detector via sheet metal to an optical post, was not rigid. Torque applied during movement into and out of the vacuum chamber caused the sheet metal to sag, creating the position shift. This was an isolated incident resulting from an initial design flaw that was later corrected for the rest of the experiment. This meant the detector was exposed to higher energy particles than intended for a given filter region. Due to this fact, this should have allowed all particles to pass through the filters unimpeded however, a cut-off point for the particles was observed in the transition between 6.5 μm and 8.5 μm

https://doi.org/10.1017/lpb.2025.10005 Published online by Cambridge University Press

Table 1. Intended designed filter setup using nominal values for filter thickness and the associated energy ranges for alpha particle transmission along with the predicted contaminated energy ranges for alpha particles that would overlap with carbon ions due to penetration through varying filter thicknesses

Filter thickness (μm)	Contaminant free α particles (MeV)	Contaminated α particles (MeV)	Carbon ions contaminants (MeV)
6.5	2.0–2.4	N/A	N/A
8.5	2.4–3.4	3.4–4.2	10.1–12.5
13.0	4.2–5.1	>5.1	>15.3

Table 2. Best estimate of filter setup that was used in the experiment, according to post-experimental measurements and analysis and the associated energy ranges for alpha particle transmission and predicted contaminated energy ranges for alpha particles that would overlap with carbon ions. The errors for all the values are also given

Filter Thickness (μm)	Contaminant free α particles (MeV)	Contaminated α particles (MeV)	Carbon ions contaminants (MeV)
$11.5^{+2.5}_{-2.8}$	$3.2^{+0.4}_{-0.5}$–$3.5^{+0.5}_{-0.6}$	N/A	N/A
$13.5^{+2.4}_{-2.7}$–$14.3^{+2.0}_{-2.4}$	$3.6^{+0.5}_{-0.6}$–$5.4^{+0.8}_{-0.9}$	$5.4^{+0.8}_{-0.9}$–$6.5^{+0.9}_{-1.1}$	$16.3^{+2.3}_{-2.8}$–$19.5^{+2.8}_{-3.3}$
$17.0^{+2.4}_{-2.4}$	N/A	$>6.8^{+1.0}_{-1.2}$	$>20.4^{+2.9}_{-3.5}$

filters. These factors prompted a direct measurement of the filter foil. A sheet of the foil from the same batch as the nominal 6.5 μm filter foil used in the proton cut-off region was measured post-experiment using a micrometer with a resolution of 1 μm. Following a careful procedure involving zeroing, consistent orientation, multiple measurements per location, and averaging across 15 distinct locations to account for surface variations, the measured thickness was determined to be 10.2 ± 1.7 μm. This value is notably higher than the nominal 6.5 μm, exceeding the range implied by the ±30% manufacturer tolerance (6.5 ± 2.0 μm), although the error bars show some overlap. This measured discrepancy is potentially attributable to factors such as foil wrinkling, which increases the effective thickness.

Using the measured thickness of 10.2 ± 1.7 μm to calibrate the magnetic field via the proton cut-off led to inconsistencies when analysing the additional cut-offs for alpha particles and carbon ions that were observed further along the trace. Ion trajectory angles (approximately 17.5° for protons) also increases the effective thickness by ∼5% over the normal thickness.

To resolve these discrepancies and account for potential in-situ effects like foil wrinkling (a phenomenon visible in Figure 1(e) near the top of the zoomed-in CR-39), the observed particle cut-offs were treated as local probes of the effective filter thickness. The calibration proceeded by assuming the effective thickness at the proton cut-off was 8.9 μm (reflecting the lower bound of the measured thickness range plus the ∼5% angular increase). This value falls within error overlaps and yields a recalculated magnetic field strength of $0.762^{+0.047}_{-0.063}$ T.

This calibrated magnetic field, when used in combination with the observed locations of the alpha and carbon cut-offs, then implied the effective filter thicknesses in the subsequent regions. These derived effective thicknesses, representing the base foil and the 2 μm foil (potentially augmented by wrinkling), were determined to be, $11.5^{+2.5}_{-2.8}$ μm (covering the first 5mm section), $13.5^{+2.4}_{-2.7}$ μm which then increases to $14.3^{+2.0}_{-2.4}$ μm further along (covering the next 15mm section) and 17 ± 2.4 μm (covering the final region, corresponding to two layers of the base foil). These derived values are physically plausible and provide a consistent explanation for all observed particle cut-offs.

Table 1 shows the designed energy ranges for alpha particle transmission through each filter thickness (using the nominal values for the filter thickness), along with the predicted energy ranges where carbon ion contamination may occur. Table 2 shows the most probable filter thicknesses based on this in-situ calibration and the consequences for filtration. The final analysis of the energy spectra presented in the Results section is based on the values from Table 2.

To allow for verification of the filters' effectiveness in eliminating carbon signals, a partial filter setup was designed for the BN target as shown in Figure 1(d). Particles produced by the laser-BN target interaction were then measured using both filtered (13 μm Al foil) and unfiltered CR-39 detectors on the TPS. Table 1 shows the designed energy ranges for alpha particle transmission through each filter thickness, along with the predicted energy ranges where carbon ion contamination may occur.

The irradiated CR-39 was then etched using a 10 mole per litre concentration solution of NaOH at a temperature of 70° C for one hour so that countable ion pits were observed. The first visible $Z/A = 0.5$ (charge to mass ratio) ion trace was observed from the B+CH target when the two CR-39s dedicated to that target were etched. The next visible $Z/A = 0.5$ ion trace was observed from the CR-39s dedicated to the BN target when those were etched.

Figure 3, which presents the raw visual data, shows a typical $Z/A = 0.5$ ion trace visible after etching a CR-39 (in this particular case, from a B+CH target). The CR-39 was then imaged using a microscope with a scale of 2.27 pixels/μm. A complete scan was then made of the $Z/A = 0.5$ ion trace that appeared in the predicted location of the alpha particles (which have $Z/A = 0.5$), based on the proton trace seen in Figure 3. Then, the resulting images were analysed using ImageJ (Ref 46) to count the number of pits with the total trace measured in slices of 700 μm. This process was repeated for the CR-39 exposed to the Al+CH reference target; however, no visible alpha particle trace was observed, as expected since the target did not contain B atoms.

Results

The first measurement was on a target of 6.5 μm thick aluminium with a layer of polyethylene deposited on top (Al+CH) with two laser shots accumulated. This had the same filter setup as the B+CH target however no alpha particles should be produced in this interaction, due to a lack of boron to initiate the p-11B reaction, meaning that any pits that are measured of similar size to the B+CH CR-39 are not from alpha particles and should be considered as background in the cases of targets containing boron. This can be argued to be the case due to the CH part of the Al+CH target, which produces the primary contaminant being investigated, carbon ions. The usage of this target for the estimation of such a background can be seen in Figure 4(a), which shows the energy spectra that would be produced if alpha particles caused these pits. The average ratio of signal to background, comparing the signal from B+CH against the background at the same energy, was 170. This was calculated by dividing the B+CH signal by the Al+CH background at each energy data point and then averaging these ratios across the entire spectrum. This ratio, being orders of magnitude higher, indicates a high significance for the results discussed in this work.

https://doi.org/10.1017/lpb.2025.10005 Published online by Cambridge University Press

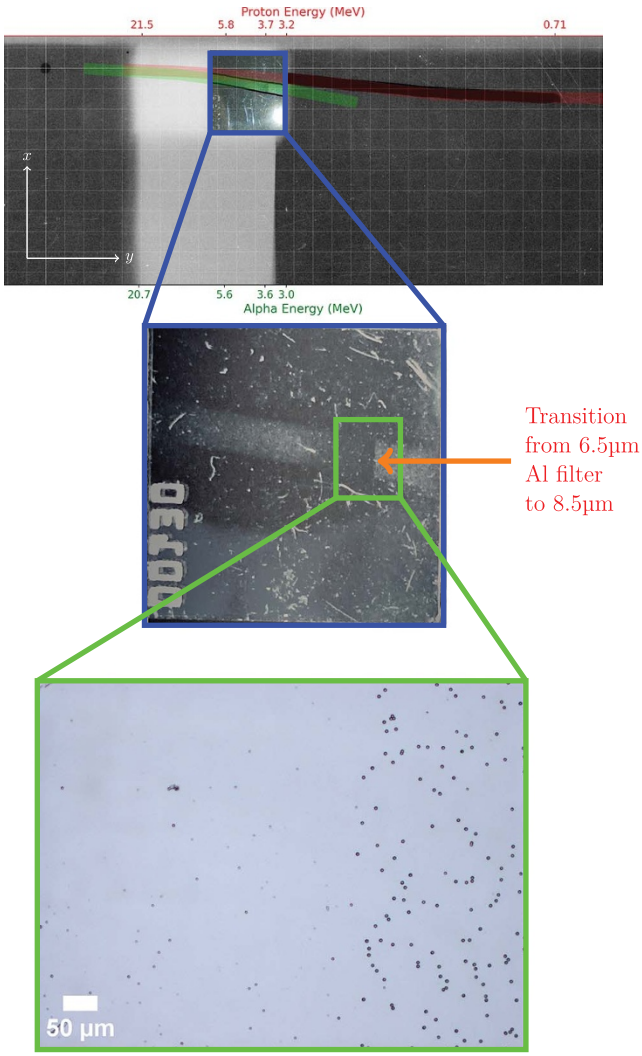

Figure 3. Image plate scan for the Boron HDPE Foam target with the associated CR-39 overlayed on top. The proton trace is predicted in red and the alpha trace is predicted in green. The dark shadow underneath the proton trace is the proton experimental signal. A zoomed-in image of the CR-39 showing the alpha trace on the CR-39. A second zoomed-in image shows a close-up of the transition of filters and the individual pits.

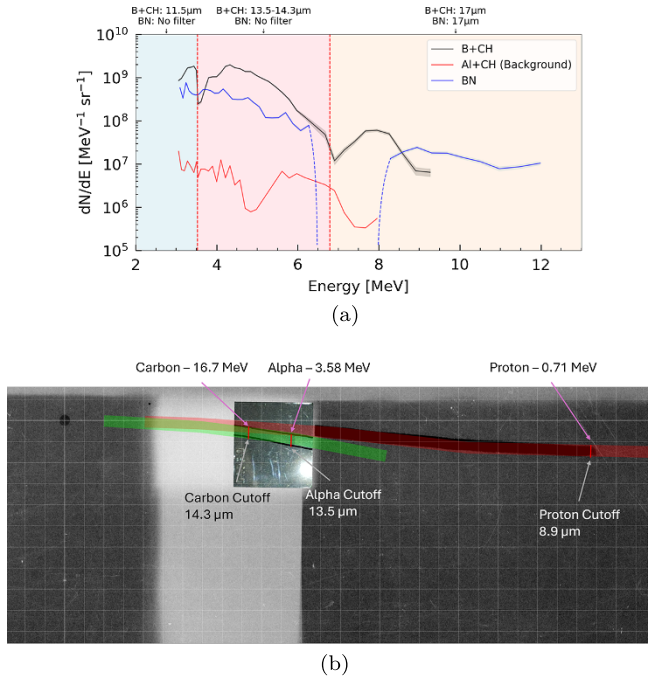

Figure 4. Alpha particle energy spectra and particle cut-off analysis. (a) Alpha particle energy spectra for both targets with the energy regions each filter covers labelled and a comparable background signal for the Boron HDPE Foam target using an Al target. The edges for the energy region for the boron nitride target, where the signal is below the typical background signal, are outlined using dashed lines. The shaded band on both spectra corresponds to the error of the energy spectrum, taking into account statistical errors, (b) The labelled locations of the three particle cut-offs observed (protons, alpha particles and carbon ions) are indicated by red lines. The identity and energy of the particles at the cut-off points are given, as well as the required aluminium thicknesses necessary to filter out lower energy particles. (a) Calculated alpha particle energy spectra for all targets, (b) Locations of particle cut-offs on the Boron HDPE Foam target along with both the energy of the particles at the cut-offs as well as the effective filter thickness.

The second measurement was performed on a B+CH target with a single laser shot. Figure 3 shows the image plate with the predicted traces for protons (red) and alpha particles (green) and includes a superimposed CR-39 photo with the visible ion trace outlined in black. The proton trace seen on the image plate did not follow the parabolic shape predicted by the TPS equations. This was because the lower energy protons were deflected by the magnetic field to such a degree along the y-axis that instead of exiting the side of the electric plate, they exited the top, meaning that they experienced a lower effective length of the electric field and thus were deflected less along the x-axis. This effect was determined by the distance in the y-axis between the pinhole and the top of the electric plate, which was found to be 47 mm. The size of the zero point spot size on the image plate is determined by three factors. The distance between the pinhole and the detector plate is divided by the distance from the target to the pinhole to get the magnification. This is multiplied by the last factor, the pinhole size, to get the zero point size. This is also the reason behind the fainter section at the end of the proton trace. The protons appear deflected by an extra 1.36 mm than expected because we detect only the one tail end of the Gaussian energy distribution for these particles, as the lower energy particles are blocked by the filter and do not overlap the signals.

The alpha particle origin of the signal is confirmed by four pieces of evidence. First, for the energy spectrum produced, three peaks can be seen in Figure 4(a) for the B+CH target, one around 3.3 MeV, the second around 3.9 MeV and the final one around 7.5 MeV. This pattern is roughly seen in other works (Refs 13, 15, 17, 26, 47), attempting to measure the energy spectrum of alpha particles from p-11B fusion, with (Ref 47) having a very similar pattern. Primarily, the region for the 3.3 and 3.9 MeV peaks appears to have been consistently measured.

These features are thus required to be intrinsic characteristics of the data for alpha particles to be responsible and not experimental artefacts. The observed dip between the 3.3 and 3.9 MeV peaks is unlikely to be solely caused by the partial transmission through the filter due to the transition from the 11.5 µm filter to the 13.5 µm filter. This is because most of the dip is far enough away from the transition for it to solely be caused by edge effects. They are also far enough apart to be distinguishable from each other, according to the resolution at that part (0.2 MeV). The effect of the filter was not removed from the energy spectra in Figure 4(a).

The second reason is based on similar experiments conducted in the past (Refs 14, 49, 56) in the same laser acceleration regime, known as Target Normal Sheath Acceleration (TNSA). In this

https://doi.org/10.1017/lpb.2025.10005 Published online by Cambridge University Press

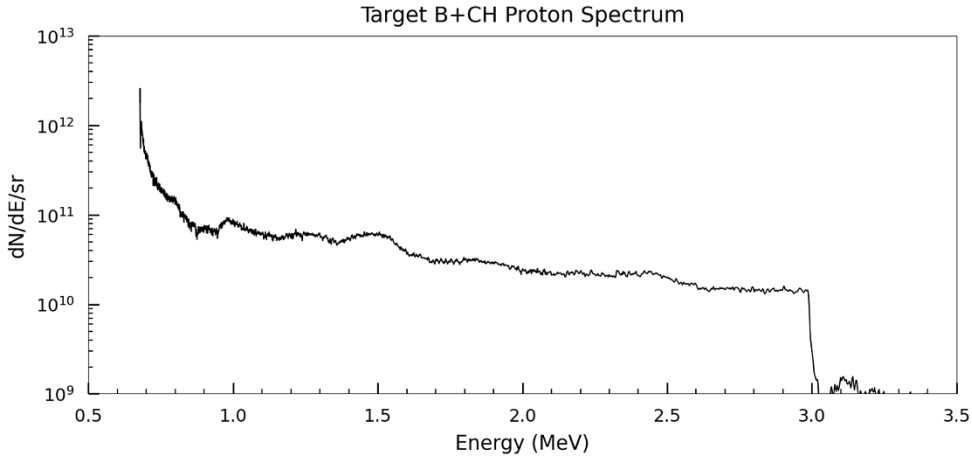

Figure 5. The proton energy spectra from the shot using the B+CH target measured using the proton trace seen on the image plate as shown in Figure 3.

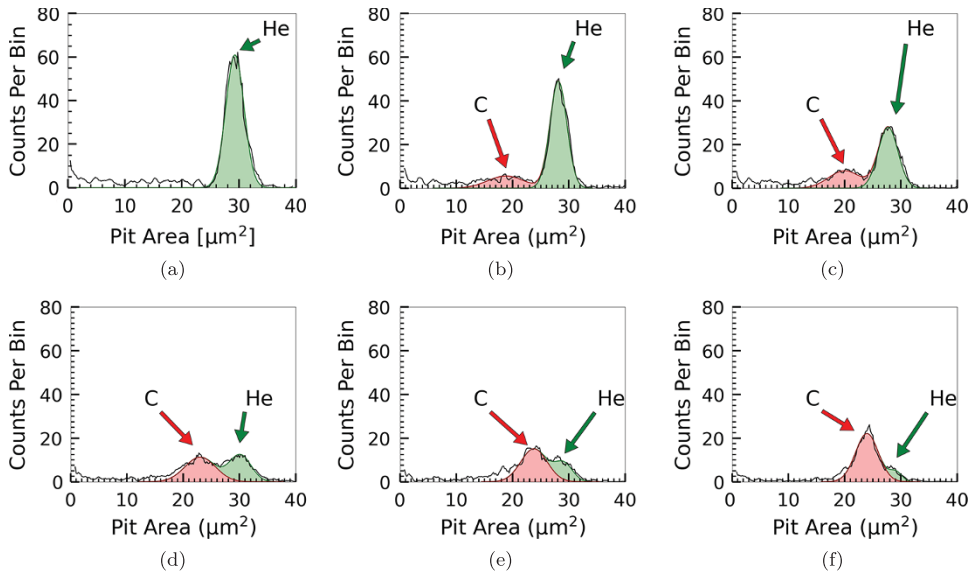

Figure 6. Graphs showing the gradual appearance and growth of a distinct carbon peak in the pit area distributions across a range of energies from the B+CH target filtered using 14.3 μm Al: (a) 5.4 MeV He, (b) 5.6 MeV He and 16.8 MeV C, (c) 5.8 MeV He and 17.4 MeV C, (d) 6.0 MeV He and 17.9 MeV C, (e) 6.2 MeV He and 18.5 MeV C, (f) 6.4 MeV He and 19.1 MeV C.

regime, the maximum energy per nucleon acquired by ions from the same accelerating potential scales with their charge-to-mass ratio. Therefore, since carbon ions have half the charge-to-mass ratio of protons, their maximum per-nucleon energy is ≈50% of a proton's.

Usually, this is even lower due to the presence of protons, producing a charge-screening effect (Ref 25) and reducing the impact the electric fields have on accelerating the carbon ions. For the B+CH target, Figure 5 displays the proton spectrum for that shot, with the highest detected energy being 3.0 MeV. This was constructed using the proton trace seen on the image plate scan for that shot, as seen in Figure 3. The intensity of this trace was then converted to the proton count using a known calibration for image plate scans. This would indicate a maximum per nucleon energy of ≈1.5 MeV for the carbon ions which is supported by the appearance of a second peak which is seen in Figure 6(b) which appears at an energy of 1.4 MeV/nucleon which is above what is capable of passing through the filter and is last seen at 1.6 MeV/nucleon. Identifying this secondary peak as carbon is important because it eliminates the most likely cause of the primary peak seen in Figure 6(b) other than alpha particles.

The third piece of evidence for alpha particle identification comes from comparing filtered and unfiltered CR-39 from the BN target. This can be seen in Figure 7, which shows pit area distributions of different regions across the two targets along with an associated picture. This is done to compare the effect the filters have on the pit size distribution, which should be comparable to the B+CH target due to containing B atoms, which should also produce alpha particles from the p-11B reaction. The filters that are present on the BN target are also in a similar position and have the same thickness as those on the B+CH target. The unfiltered CR-39 exposed to the BN target, shown in Figure 7(d), displays multiple peaks in the size distribution, indicating the presence of various ion species, including carbon. However, when examining the filtered CR-39 in Figure 7(c), only a single peak remains. This shows the effectiveness of the filters to remove various ion species,

https://doi.org/10.1017/lpb.2025.10005 Published online by Cambridge University Press

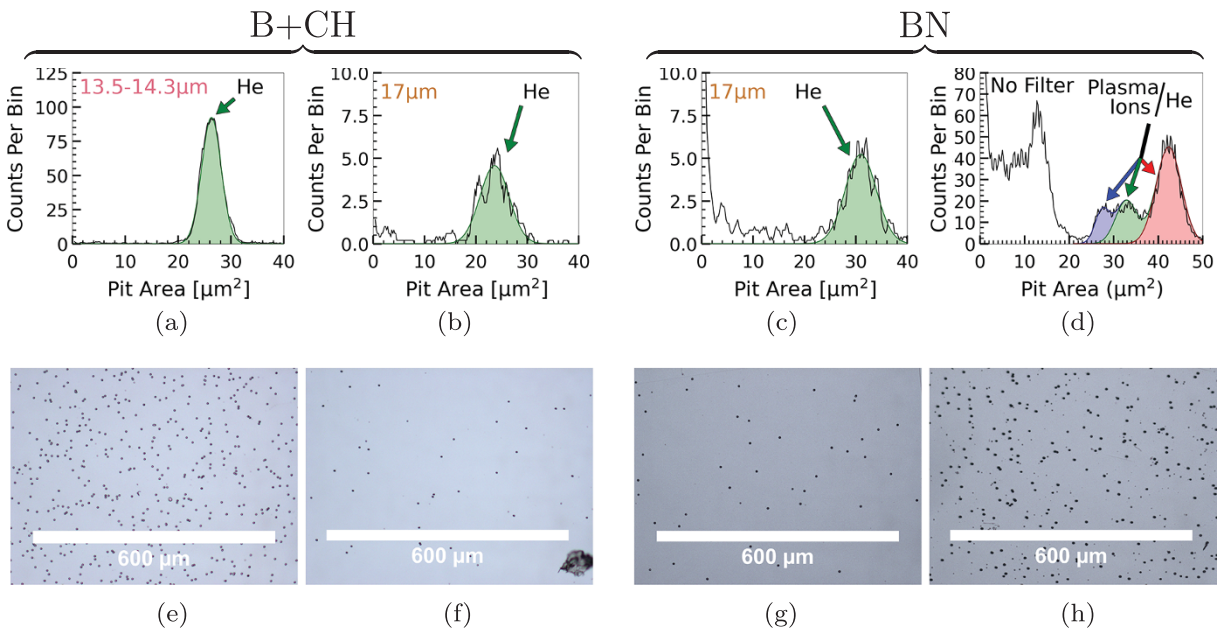

Figure 7. Graphs showing the pit area distribution on the CR-39s smoothed out with a moving average of 5 points and overlaid with a Gaussian curve fitted against the raw data. (a) and (e) displays information on the 13.5–14.3 μm filtered pits seen from the Boron HDPE Foam target at an alpha energy of 4.8 MeV where a prominent, easily defined peak is seen, (b) and (f) displays information on the 17 μm filtered pits seen at alpha energy 8.3 MeV from a Boron HDPE Foam target, (c) and (g) displays information on the 17 μm filtered pits seen at alpha energy 9.3 MeV from a Boron Nitride target and (d) and (h) displays information on the non-filtered pits seen at alpha energy 5.5 MeV from a Boron Nitride target that has multiple peaks from different ion species: (a) Pit area distribution: 4.8 MeV He from filtered B+CH, (b) Pit area distribution: 8.3 MeV He from filtered B+CH, (c) Pit area distribution: 9.3 MeV He from filtered BN, (d) Pit area distribution: 5.5 MeV He and 16.6 MeV C from non-filtered BN, (e) Pits from filtered B+CH: 4.8 MeV He, (f) Pits from filtered B+CH: 8.3 MeV He, (g) Pits from filtered BN: 9.3 MeV He, (h) Pits from non-filtered BN: 5.5 MeV He and 16.6 MeV C.

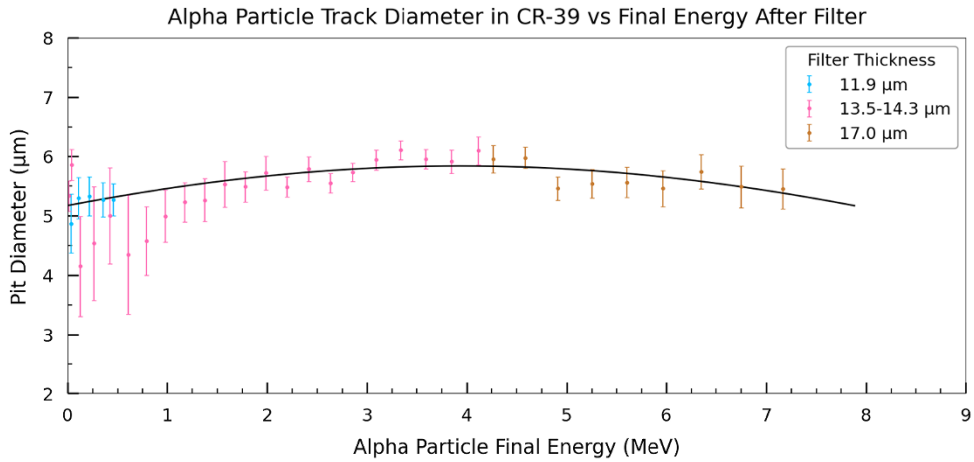

Figure 8. Graph showing the pattern in alpha particle track diameters in CR-39 against incident alpha particle energy at the CR-39 surface, measured using filters of varying thickness (11.5, 13.5–14.3, 17.0 μm). Tracks were produced by etching in 10 mole/L NaOH solution for 1 hour, with initial source energies measured using the TPS and then adjusted to account for energy loss through the filters.

leaving only one ion species (alpha particles) to penetrate through. This surviving peak must correspond to an ion species lighter than that which was filtered out. This peak can be compared to the peak of similar energy in the same filter region on the CR-39 from the B+CH target seen in Figure 7(b).

The surviving peak (shown in green) is transmitted through the 13.5–14.3 μm filter at energies as low as 0.9 MeV/nucleon, while a separate peak (shown in red in Figure 6(b)) only appears at 1.4 MeV/nucleon. Given that boron and carbon ions have similar penetration depths (as demonstrated in Figure 2), if the green peak represented boron ions, we would expect to see the carbon peak (red) at substantially lower energies. The observed energy gap between these peaks is consistent with the difference in penetration depths between alpha particles and heavier ions (boron/carbon), strongly suggesting that alpha particles are responsible for the green peak.

Finally, the relationship observed between the alpha particle pit size on the CR-39 and the particle's energy is consistent with previous CR-39 calibration studies (Refs 4, 44, 58). Figure 8 plots the diameter of the pits against the energy of the alpha particles after they passed through the filters and struck the CR-39 surface. This final energy was calculated using the known filter thicknesses to determine the energy lost by the particles. Each data point in Figure 8 corresponds to a specific segment of the alpha particle

https://doi.org/10.1017/lpb.2025.10005 Published online by Cambridge University Press

trace. The points are divided into three categories based on the filter used for that segment. These calibration studies (Refs 4, 44, 58) typically show that alpha particle pit sizes peak at energies around 3–4 MeV before decreasing. This differs from carbon ions, which generally produce larger pits at higher energies.

The energy resolution for the TPS can be calculated using equation (3) shown below (Ref 20):

$$\frac{\Delta E}{E} \approx \frac{2\Delta x}{x}, \tag{3}$$

where ΔE is the energy resolution, E is the particle's energy, Δx is the zero point spot size on the image plate (1.36 mm radius), and x is the deflection along the magnetic axis. Using this, the resolution at 3.0 MeV for the boron HDPE foam target can be calculated to be ±0.1 MeV and at 8.0 MeV it is ±0.6 MeV.

The third measurement was on a BN target fired upon with two laser shots accumulated on it. The filters used were different from the previous set of results, with no filters used in the first 20 mm of CR-39 and then 17 μm Al used for the next 20 mm. Higher alpha particle energies were seen in Figure 4(a) for the BN target compared to the B+CH target and could be explained by the production of higher energy protons with a relative deficit of the lower energy protons produced to pair with the low energy reaction cross-section peaks for the p-11B reaction.

This set of results combines the more traditional CR-39 method and the novel technique described in this paper. This allows for the demonstration of the clear distinction and measurement of alpha particles that are possible with the removal of the various contaminants found, such as carbon ions as shown in Figure 7(c) and (d).

For the primary B+CH target, approximately 40,000 pits were observed, which translates to an alpha yield of $3.4 \pm 0.1 \times 10^9$ particles/sr. For the BN target, ∼25,000 pits (accumulated over two shots) correspond to a yield of $1.04 \pm 0.02 \times 10^9$ particles/sr. The background, measured with the Al+CH target, was $1.01 \pm 0.03 \times 10^8$ particles/sr. This results in signal-to-noise ratios of approximately 34 for the B+CH target and a much lower ratio of about 10 for the BN target.

Conclusions

In this work, we have demonstrated a novel approach to discriminate and measure, for the first time, alpha particles in laser-driven proton-boron fusion experiments using a CR-39 enhanced Thomson parabola spectrometer (TPS) coupled with differential filtering. This technique eliminated background contamination from plasma ions across a large proportion of the measured energy spectrum. In particular, carbon ions were removed, which typically overlap with the alpha particle trace on the TPS. By employing aluminium foils of varying thicknesses (11.5, 13.5–14.3 and 17 μm) along the energy dispersion axis of the TPS, we were able to generate a quasi-contaminant-free alpha particle energy spectrum, following careful post-hoc calibration, for a foam boron target. The spectrum covered an energy range of 3-8 MeV with two types of errors that affected the energy levels in different ways. The first is the energy resolution of ±0.1 MeV at 3.0 MeV up to ±0.5 MeV at 8.0 MeV between data points. This type affected the ability to distinguish features in the energy spectrum. The second error type is due to the magnetic field intensity accuracies, which caused errors of $3.0^{+0.4}_{-0.5}$ MeV and $8.0^{+1.0}_{-1.3}$ MeV. This error type affected how much the entire energy spectrum was stretched and shifted in one direction in the TP spectrometer. The combined error for a given energy point was $3.0^{+0.4}_{-0.5}$ MeV at one end and $8.0^{+1.2}_{-1.4}$ MeV at the other.

The results obtained from the boron nitride (BN) and boron HDPE foam (B+CH) targets demonstrated the effectiveness of the differential filtering method in eliminating the contribution of carbon ions to the alpha particle signal. The aluminium polyethylene (Al+CH) reference target, which was not expected to produce alpha particles, served as a control to validate the technique as well as determine the signal-to-noise ratio of the measured result. The enhanced detection sensitivity provided by the CR-39 detector, compared to a conventional image plate, is another significant advantage of this technique. Due to the high energy resolution of this method, fine spectral features in the alpha particle measurements can be detected. This could return key information that allows for the kinematics of pB fusion to be reconstructed. This novel approach has the potential to measure even lower energy ranges of alpha particles, further extending its applicability in laser-driven fusion experiments, dependent on the availability of filters that must be both extremely thin and manufactured with tight thickness tolerances.

Crucially important to the practical application of this diagnostic is ensuring a low error in the thickness of the filters used. Particularly for lower-energy particles, such as 2 MeV alpha particles, the difference in penetration for alpha particles and other plasma ions can be as little as 1 μm. Thus, future research should use filters with a better tolerance on their thickness than is more commercially available. A smooth, flat fit against whatever surface the filter is placed against must also be guaranteed.

A larger detected energy range of alpha particles should also be possible by placing an additional CR-39 for even lower energies. A better balancing act should also be made between the y- and x-axis errors of the energy spectrum by decreasing the pinhole size to reduce the energy error, as the particle flux error or y-axis error was unnecessarily small. Every effort should be made to reduce the distance between the TPS and the target, since a smaller pinhole size reduces the number of alpha particles passing through, making detection more difficult on the CR-39 and increasing the y-axis error. These issues can be mitigated by ensuring a large solid angle for the diagnostic. A small solid angle could also be more susceptible to particle flux variations when attempting to calculate the yield of the source target. For a more accurate estimation of the overall flux, detectors with a large sensitive area can be used, such as bare CR39, used in similar conditions (Ref 33).

The ability to fully utilise this technique to optimise the laser parameters to increase alpha production is limited by the long analysis period required for CR-39. A better version of the technique would be to replace both the image plate and CR-39 with a time of flight (TOF) detector array (Ref 28). If a sufficiently high electric field is used to separate the proton and alpha and the TOF is placed accurately with differential filters known to a high accuracy of thickness, then it is possible to obtain a pure alpha signal with the ability to create the alpha energy spectrum for each laser shots, even those with high rep rates in the kHz regime. If enhanced by using a Timepix detector (Ref 12), to differentiate the signal along the y-axis of the TPS, this could also provide an independent measurement of the energy level of the alpha particles. This would allow for the fine attunement of laser parameters such as focus, pulse length and energy to obtain the highest alpha production rate. However, the detector should be properly shielded from electromagnetic pulses (EMP) (Ref 11) and getting the correct balance between placing it near the target to have a high number of

https://doi.org/10.1017/lpb.2025.10005 Published online by Cambridge University Press

alpha particles detected for the y-axis error and moving it further away to have a low energy level error in the x-axis.

In conclusion, the proposed CR-39 enhanced TPS with differential filtering has proven to be a powerful diagnostic tool for accurate discrimination and measurement of alpha particles in laser-driven proton-boron fusion experiments. This technique opens up new possibilities for understanding the reaction dynamics and optimising the fusion process, which is crucial for the development of laser-plasma schemes for energy production.

Acknowledgements. The corresponding author wishes to thank his fellow PhD students for the assistance provided during the experiment. The PhD under which this paper was written was funded by a Department for the Economy (DfE) studentship. This work received support from COST Action CA21128-PROBONO "PROton BOron Nuclear fusion: from energy production to medical applicatiOns", supported by COST (European Cooperation in Science and Technology). This work has been partially carried out within the framework of the EUROfusion Consortium, funded by the European Union via the Euratom Research and Training Programme (Grant Agreement No 101052200 — EUROfusion). Views and opinions expressed are however those of the authors only and do not necessarily reflect those of the European Union or the European Commission. Neither the European Union nor the European Commission can be held responsible for them. This work was also supported by the Czech Science Foundation through the grant GACR24-11398S.

References

1. **Alejo A, Kar S, Ahmed H, Krygier AG, Doria D, Clarke R, Fernandez J, Freeman RR, Fuchs J, Green A, Green JS, Jung D, Kleinschmidt A, Lewis CLS, Morrison JT, Najmudin Z, Nakamura H, Nersisyan G, Norreys P, Notley M, Oliver M, Roth M, Ruiz JA, Vassura L, Zepf M and Borghesi M** (2014) Characterisation of deuterium spectra from laser driven multi-species sources by employing differentially filtered image plate detectors in Thomson spectrometers. *Review of Scientific Instruments* **85**(9), 093303. https://doi.org/10.1063/1.4893780
2. **Alejo A, Kar S, Tebartz A, Ahmed H, Astbury S, Carroll DC, Ding J, Doria D, Higginson A, McKenna P, Neumann N, Scott GG, Wagner F, Roth M and Borghesi M** (2016) High resolution Thomson Parabola Spectrometer for full spectral capture of multi-species ion beams. *Review of Scientific Instruments* **87**(8), 083304. https://doi.org/10.1063/1.4961028
3. **Baccou C, Depierreux S, Yahia V, Neuville C, Goyon C, De Angelis R, Consoli F, Ducret JE, Boutoux G, Rafelski J and Labaune C** (2015a) New scheme to produce aneutronic fusion reactions by laser-accelerated ions. *Laser and Particle Beams* **33**(1), 117–122. https://doi.org/10.1017/S0263034615000178
4. **Baccou C, Yahia V, Depierreux S, Neuville C, Goyon C, Consoli F, De Angelis R, Ducret JE, Boutoux G, Rafelski J and Labaune C** CR-39 track detector calibration for H, He and C ions from 0.1-0.5 MeV up to 5 MeV for laser-induced nuclear fusion product identification. *Review of Scientific Instruments* **86**(8), 2015b. https://doi.org/10.1063/1.4927684
5. **Bonvalet J, Nicolaï P, Raffestin D, D'humieres E, Batani D, Tikhonchuk V, Kantarelou V, Giuffrida L, Tosca M, Korn G, Picciotto A, Morace A, Abe Y, Arikawa Y, Fujioka S, Fukuda Y, Kuramitsu Y, Habara H and Margarone D** (2021) Energetic α-particle sources produced through proton-boron reactions by high-energy high-intensity laser beams. *Physical Review E* **103**(5), 053202. https://doi.org/10.1103/PhysRevE.103.053202
6. **Burdiak GC, Skidmore JW, Allison JR, Barker RL, Doyle HW, Escauriza EM, Niasse N-PL, Peši' Z, Ringrose TJ, Hawker NA** Validate production of neutrons from gas gun-driven targets. Technical report, First Light Fusion Ltd. 2022. Available at: https://firstlightfusion.com/science-hub/validate-production-of-neutrons-from-gas-gun-driven-targets/
7. **Cassou RM and Benton EV** (1978) Properties and applications of CR-39 polymeric nuclear track detector. *Nuclear Track Detection* **2**(3), 173–179. https://doi.org/10.1016/0145-224x(78)90021-2
8. **Cirrone GAP, Manti L, Margarone D, Petringa G, Giuffrida L, Minopoli A, Picciotto A, Russo G, Cammarata F, Pisciotta P, Perozziello FM, Romano F, Marchese V, Milluzzo G, Scuderi V, Cuttone G and Korn G** (2018) First experimental proof of Proton Boron Capture Therapy (PBCT) to enhance protontherapy effectiveness. *Scientific Reports* **8**(1), 1141. https://doi.org/10.1038/s41598-018-19258-5
9. **Cobble JA, Flippo KA, Offermann DT, Lopez FE, Oertel JA, Mastrosimone D, Letzring SA and Sinenian N** (2011) High-resolution Thomson parabola for ion analysis. *Review of Scientific Instruments* **82**(11), 113504. https://doi.org/10.1063/1.3658048
10. **Consoli F, De Angelis R, Andreoli P, Bonasera A, Cipriani M, Cristofari G, Di Giorgio G, Giulietti D and Salvadori M** Diagnostic methodologies of laser-initiated 11B(p,α)2α fusion reactions. *Frontiers in Physics* **8** 2020a. https://doi.org/10.3389/fphy.2020.561492
11. **Consoli F, Tikhonchuk VT, Bardon M, Bradford P, Carroll DC, Cikhardt J, Cipriani M, Clarke RJ, Cowan TE, Danson CN, De Angelis R, De Marco M, Dubois J-L, Etchessahar B, Garcia AL, Hillier DII, Honsa A, Jiang W, Kmetik V, Krása J, Yutong L, Lubrano F, McKenna P, Metzkes-Ng J, Poyé A, Prencipe I, Raczka P, Smith RA, Vrana R, Woolsey NC, Zemaityte E, Zhang Y, Zhang Z, Zielbauer B and Neely D** (2020b) Laser produced electromagnetic pulses: generation, detection and mitigation. *High Power Laser Science and Engineering* **8**, e22. https://doi.org/10.1017/hpl.2020.13
12. **Gehrke T, Gallas R, Jäkel O and Martišíková M** (2018) Proof of principle of helium-beam radiography using silicon pixel detectors for energy deposition measurement, identification, and tracking of single ions. *Medical Physics* **45**(2), 817–829. https://doi.org/10.1002/mp.12723
13. **Giuffrida L, Belloni F, Margarone D, Petringa G, Milluzzo G, Scuderi V, Velyhan A, Rosinski M, Picciotto A, Kucharik M, Dostal J, Dudzak R, Krasa J, Istokskaia V, Catalano R, Tudisco S, Verona C, Jungwirth K, Bellutti P, Korn G and Cirrone GAP** (2020) High-current stream of energetic α particles from laser-driven proton-boron fusion. *Physical Review E* **101**(1), 013204. https://doi.org/10.1103/PhysRevE.101.013204
14. **Hegelich M, Karsch S, Pretzler G, Habs D, Witte K, Guenther W, Allen M, Blazevic A, Fuchs J, Gauthier JC, Geissel M, Audebert P, Cowan T and Roth M** (2002) MeV ion jets from short-pulse-laser interaction with thin foils. *Physical Review Letters* **89**(8), 085002. https://doi.org/10.1103/PhysRevLett.89.085002
15. **Huault M, Carrière T, Larreur H, Nicolaï P, Raffestin D, Singappuli D, D'Humieres E, Dubresson D, Batani K, Cipriani M, Filippi F, Scisciò M, Verona C, Giuffrida L, Kantarelou V, Stancek S, Boudjema N, Lera R, Pérez-Hernández JA, Volpe L, Rodríguez Frías MD, Bonasera A, Rodrigues MRD, Chavez DR, Consoli F and Batani D** (2025) Experimental and computational evaluation of alpha particle production from laser-driven proton–boron nuclear reaction in hole-boring scheme. *Physics of Plasmas* **32**(1), 013102. https://doi.org/10.1063/5.0238029
16. **Ignatov I and Mosin O** (2013) Modeling of possible processes for origin of life and living matter in hot mineral and seawater with deuterium. *Journal of Environment and Earth Science* **3**(14), 103–118
17. **Istokskaia V, Tosca M, Giuffrida L, Psikal J, Grepl F, Kantarelou V, Stancek S, Di Siena S, Hadjikyriacou A, McIlvenny A, Levy Y, Huynh J, Cimrman M, Pleskunov P, Nikitin D, Choukourov A, Belloni F, Picciotto A, Kar S, Borghesi M, Lucianetti A, Mocek T and Margarone D** (2023) A multi-MeV alpha particle source via proton-boron fusion driven by a 10-GW tabletop laser. *Communications Physics* **6**(1), 27. https://doi.org/10.1038/s42005-023-01135-x
18. **ITER Organization**. Tritium breeding. ITER Organization. Available at: https://www.iter.org/mach/TritiumBreeding
19. **James FZ, Ziegler MD and Biersack JP** (2010) SRIM – the stopping and range of ions in matter (2010). *Nuclear Instruments and Methods in Physics Research Section B: Beam Interactions With Materials and Atoms* **268**(11-12), 1818–1823. https://doi.org/10.1016/j.nimb.2010.02.091
20. **Jung D, Hörlein R, Kiefer D, Letzring S, Gautier DC, Schramm U, Hübsch C, Öhm R, Albright BJ, Fernandez JC, Habs D and Hegelich BM** (2011) Development of a high resolution and high dispersion Thomson parabola. *Review of Scientific Instruments* **82**(1), 013306. https://doi.org/10.1063/1.3523428
21. **Kantarelou V, Velyhan A, Tchórz P, Rosiński M, Petringa G, Cirrone GAP, Istokskaia V, Krása J, Krůs M, Picciotto A, Margarone D,**

Giuffrida L and Pikuz S (2023) A methodology for the discrimination of alpha particles from other ions in laser-driven proton-boron reactions using CR-39 detectors coupled in a thomson parabola spectrometer. *Laser and Particle Beams* **2023** e10. https://doi.org/10.1155/2023/3125787

22. **Katarzyna Liliana Batani MRDR, Bonasera A, Cipriani M, Consoli F, Filippi F, Scisciò M, Giuffrida L, Kantarelou V, Stancek S, Lera R, Pérez-Hernández JA, Volpe L, Turcu E, Passoni M, Vavassori D, Dellasega D, Maffini A, Huault M, Larreur H, Sayo L, Carriere T, Nicolai P, Raffestin D, Singappuli D and Batani D** (2025) Generation of radioisotopes for medical applications using high-repetition, high-intensity lasers. *High Power Laser Science and Engineering* **13**, 1–25. https://doi.org/10.1017/hpl.2024.92
23. **Kirtley D and Milroy R** (2023) Fundamental scaling of adiabatic compression of field reversed configuration thermonuclear fusion plasmas. *Journal of Fusion Energy* **42**(2), 30. https://doi.org/10.1007/s10894-023-00367-7
24. **Lucas LL and Unterweger MP** (2000) Comprehensive review and critical evaluation of the half-life of tritium. *Journal of Research of the National Institute of Standards and Technology* **105**(4), 541. https://doi.org/10.6028/jres.105.043
25. **Macchi A, Borghesi M and Passoni M** (2013) Ion acceleration by superintense laser-plasma interaction. *Reviews of Modern Physics* **85**(2), 751–793. https://doi.org/10.1103/RevModPhys.85.751
26. **Margarone D, Bonvalet J, Giuffrida L, Morace A, Kantarelou V, Tosca M, Raffestin D, Nicolai P, Picciotto A, Abe Y, Arikawa Y, Fujioka S, Fukuda Y, Kuramitsu Y, Habara H and Batani D** (2022) In-target proton–boron nuclear fusion using a PW-class laser. *Applied Sciences* **12**(3), 1444. https://doi.org/10.3390/app12031444
27. **Margarone D, Krasa J, Picciotto A, Torrisi L, Laska L, Velyhan A, Prokupek J, Ryc L, Parys P, Ullschmied J and Rus B** (2011a) High current, high energy proton beams accelerated by a sub-nanosecond laser. *Nuclear Instruments and Methods in Physics Research Section A: Accelerators, Spectrometers, Detectors and Associated Equipment* **653**(1), 159–163. https://doi.org/10.1016/j.nima.2010.12.118
28. **Margarone D, Krasa J, Giuffrida L, Picciotto A, Torrisi L, Nowak T, Musumeci P, Velyhan A, Prokpek J, Lska L, Mocek T, Ullschmied J and Rus B** Full characterization of laser-accelerated ion beams using Faraday cup, silicon carbide, and single-crystal diamond detectors. *Journal of Applied Physics* **109**(10), 2011b. https://doi.org/10.1063/1.3585871
29. **Margarone D, Morace A, Bonvalet J, Abe Y, Kantarelou V, Raffestin D, Giuffrida L, Nicolai P, Tosca M, Picciotto A, Petringa G, Cirrone GAP, Fukuda Y, Kuramitsu Y, Habara H, Arikawa Y, Fujioka S, D'Humieres E, Korn G and Batani D** (2020) Generation of α-particle beams with a multi-kJ, peta-watt class laser system. *Frontiers in Physics* **8**, 343. https://doi.org/10.3389/fphy.2020.00343
30. **McKenzie W, Batani D, Mehlhorn TA, Margarone D, Fabio Belloni EMC, Woodruff S, Kirchhoff J, Paterson A, Pikuz S and Hora H** (2023) HB11 – understanding hydrogen-boron fusion as a new clean energy source. *Journal of Fusion Energy* **42**(1), 17. https://doi.org/10.1007/s10894-023-00349-9
31. **Meschini S, Laviano F, Ledda F, Pettinari D, Testoni R, Torsello D and Panella B** (2023) Review of commercial nuclear fusion projects. *Frontiers in Energy Research* **11** 1157394. https://doi.org/10.3389/fenrg.2023.1157394
32. **Heindler M and Kernbichler W** (1989) Advanced Fuel Fusion. *Emerging Nuclear Energy Systems 1989: Proceedings of the fifth International Conference on Emerging Nuclear Energy Systems*. In Mollendorff UV and Goel B, 177–182. Teaneck, NJ: World Scientific, F.R. germany, july 3-6, 1989.
33. **Molloy DP, Orecchia D, Tosca M, Milani A, Valt M, McNamee A, Fitzpatrick CRJ, Kantarelou V, Kennedy JP, Martin P, Nersisyan G, Biliak K, Protsak M, Nikitin D, Borghesi M, Choukourov A, Giuffrida L, Kar S, Maffini A, Passoni M, Picciotto A and Margarone D** (2025) Alpha particle production from novel targets via laser-driven proton-boron fusion. *Physical Review Research* **7**(1), 013230. https://doi.org/10.1103/PhysRevResearch.7.013230
34. **Morris AW, Akers RJ, Cox M, Militello F, Surrey E, Waldon CW, Wilson HR and Zohm H** (2022) Towards a fusion power plant: integration of physics and technology. *Plasma Physics and Controlled Fusion* **64**(6), 064002. https://doi.org/10.1088/1361-6587/ac6694
35. **Muyi N, Wang Y, Yuan B, Jiang J and Yican W** (2013) Tritium supply assessment for ITER and DEMOnstration power plant. *Fusion Engineering and Design* **88**(9–10), 2422–2426. https://doi.org/10.1016/j.fusengdes.2013.05.043
36. **Orecchia D, Maffini A, Zavelani-Rossi M and Passoni M** (2024) Versatile synthesis of nanofoams through femtosecond pulsed laser deposition. *Small Structures* **5**(6), 2300560. https://doi.org/10.1002/sstr.202300560
37. **Otuka N, Dupont E, Semkova V, Pritychenko B, Blokhin AI, Aikawa M, Babykina S, Bossant M, Chen G, Dunaeva S, Forrest RA, Fukahori T, Furutachi N, Ganesan S, Ge Z, Gritzay OO, Herman M, Hlavač S, Katō K, Lalremruata B, Lee YO, Makinaga A, Matsumoto K, Mikhaylyukova M, Pikulina G, Pronyaev VG, Saxena A, Schwerer O, Simakov SP, Soppera N, Suzuki R, Takács S, Tao X, Taova S, Tárkányi F, Varlamov VV, Wang J, Yang SC, Zerkin V and Zhuang Y** (2014) Towards a more complete and accurate experimental nuclear reaction data library (EXFOR): International collaboration between nuclear reaction data centres (NRDC). *Nuclear Data Sheets* **120**, 272–276. https://doi.org/10.1016/j.nds.2014.07.065
38. **Park SJ, Jang JG and Lee HK** (2014) Computational investigation of the neutron shielding and activation characteristics of borated concrete with polyethylene aggregate. *Journal of Nuclear Materials* **452**(1-3), 205–211. https://doi.org/10.1016/j.jnucmat.2014.05.010
39. **Pearson RJ, Antoniazzi AB and Nuttall WJ** (2018) Tritium supply and use: a key issue for the development of nuclear fusion energy. *Fusion Engineering and Design* **136**, 1140–1148. https://doi.org/10.1016/j.fusengdes.2018.04.090
40. **Phillips J.E. Easterly C.E.**. Sources of tritium. Technical report, Oak Ridge National Laboratory (ORNL), Oak Ridge, TN (United States), 1980
41. **Qaim SM, Spahn I, Scholten B and Neumaier B** (2016) Uses of alpha particles, especially in nuclear reaction studies and medical radionuclide production. *Radiochimica Acta* **104**(9), 601–624. https://doi.org/10.1515/ract-2015-2566
42. **Rodrigues MRD, Bonasera A, Scisciò M, Pérez-Hernández JA, Ehret M, Filippi F, Andreoli PL, Huault M, Larreur H, Singappuli D, Molloy D, Raffestin D, Alonzo M, Rapisarda GG, Lattuada D, Guardo GL, Verona C, Consoli F, Petringa G, McNamee A, Cognata ML, Palmerini S, Carriere T, Cipriani M, Di Giorgio G, Cristofari G, De Angelis R, Cirrone GAP, Margarone D, Giuffrida L, Batani D, Nicolai P, Batani K, Lera R, Volpe L, Giulietti D, Agarwal S, Krupka M, Singh S and Consoli F** (2024) Radioisotope production using lasers: From basic science to applications. *Matter and Radiation at Extremes* **9**(3), 037203. https://doi.org/10.1063/5.0196909
43. **Rubel M** (2018) Fusion neutrons: Tritium breeding and impact on wall materials and components of diagnostic systems. *Journal of Fusion Energy* **38**(3–4), 315–329. https://doi.org/10.1007/s10894-018-0182-1
44. **Sadowski M, Szydlowski A, Jaskola M, Czyzewski T and Kobzev AP** (1997) Comparison of responses of CR-39, PM-355, and CN track detectors to energetic hydrogen-, helium-, nitrogen-, and oxygen-ions. *Radiation Measurements* **28**(1-6), 207–210 https://doi.org/10.1016/S1350-4487(97)00069-3
45. **Salvadori M, Scisciò M, Di Giorgio G, Cipriani M, Andreoli PL, Cristofari G, De Angelis R, Giulietti D, Consoli F and Margarone D** (2023) Univocal discrimination of α particles produced by 11B(p, α)2α fusions in laser-matter experiments by advanced thomson spectrometry. *Laser and Particle Beams* **2023**, 6. https://doi.org/10.1155/2023/7831712
46. **Schneider CA, Rasband WS and Eliceiri KW** (2012) NIH Image to ImageJ: 25 years of image analysis. *Nature Methods* **9**(7), 671–675. https://doi.org/10.1038/nmeth.2089
47. **Scisciò M, Petringa G, Zhu Z, Rodrigues MRD, Alonzo M, Andreoli PL, Filippi F, Consoli F, Huault M, Raffestin D, Molloy D, Larreur H, Singappuli D, Carriere T, Verona C, Nicolai P, McNamee A, Ehret M, Filippov E, Lera R, Pérez-Hernández JA, Agarwal S, Krupka M, Singh S, Istokskaia V, Lattuada D, Cognata ML, Guardo GL, Palmerini S, Rapisarda G, Batani K, Cipriani M, Cristofari G, Di Ferdinando E, Di Giorgio G, De Angelis R, Giulietti D, Xu J,**

Volpe L, Rodríguez-Frías MD, Giuffrida L, Margarone D, Batani D, Cirrone GAP, Bonasera A and Consoli F (2025) Laser-initiated p–11B fusion reactions in petawatt high-repetition-rate laser facilities. *Matter and Radiation at Extremes* **10**(3), 037402. https://doi.org/10.1063/5.0241993

48. **Scott CH** (2023) U.S. fusion energy development via public-private partnerships. *Journal of Fusion Energy* **42**(1), 12. https://doi.org/10.1007/s10894-023-00357-9
49. **Scullion C, Doria D, Romagnani L, Sgattoni A, Naughton K, Symes DR, McKenna P, Macchi A, Zepf M, Kar S and Borghesi M** (2017) Polarization dependence of bulk ion acceleration from ultrathin foils irradiated by high-intensity ultrashort laser pulses. *Physical Review Letters* **119**(5), 054801. https://doi.org/10.1103/PhysRevLett.119.054801
50. **Seo J, Kim SK, Jalalvand A, Conlin R, Rothstein A, Abbate J, Erickson K, Wai J, Shousha R and Kolemen E** (2024) Avoiding fusion plasma tearing instability with deep reinforcement learning. *Nature* **626**(8000), 746–751. https://doi.org/10.1038/s41586-024-07024-9
51. **Stambaugh RD, Chan VS, Miller RL and Schaffer MJ** (1998) The spherical tokamak path to fusion power. *Fusion Technology* **33**(1), 1–21 https://doi.org/10.13182/FST33-1
52. **Tayeb MB, Tikhonchuk V and Feugeas J-L** (2024) ICF target optimization using generative AI. *Physics of Plasmas* **31**(10), 103903. https://doi.org/10.1063/5.0228824
53. **Thomson JJ** (1913) Bakerian Lecture: Rays of positive electricity. *Proceedings of the Royal Society of London. Series A, Containing Papers of a Mathematical and Physical Character* **89**(607), 1–20. https://doi.org/10.1098/rspa.1913.0057
54. **Tran NH, Shtam T, Marchenko YY, Konevega AL and Lebedev D** (2023) Current state and prospectives for proton boron capture therapy. *Biomedicines* **11**(6), 1727. https://doi.org/10.3390/biomedicines11061727
55. **UKAEA** (2024) Fusion research facility JET's final tritium experiments yield new energy record. CCFE UKAEA. Available at: https://ccfe.ukaea.uk/fusion-research-facility-jets-final-tritium-experiments-yield-new-energy-record/
56. **Wilks SC, Langdon AB, Cowan TE, Roth M, Singh M, Hatchett S, Key MH, Pennington D, MacKinnon A and Snavely RA** (2001) Energetic proton generation in ultra-intense laser–solid interactions. *Physics of Plasmas* **8**(2), 542–549. https://doi.org/10.1063/1.1333697
57. **Yamauchi T** (2003) Studies on the nuclear tracks in CR-39 plastics. *Radiation Measurements* **36**(1-6), 73–81. https://doi.org/10.1016/S1350-4487(03)00099-4
58. **Zhang Y, Wang H-W, Yu-Gang M, Liu L-X, Cao X-G, Fan G-T, Zhang G-Q and Fang D-Q** (2019) Energy calibration of a CR-39 nuclear-track detector irradiated by charged particles. *Nuclear Science and Techniques* **30**(6), 87. https://doi.org/10.1007/s41365-019-0619-x

https://doi.org/10.1017/lpb.2025.10005 Published online by Cambridge University Press